Mesoscale variability of the summer bloom over the northern Ross Sea Shelf: A Tale of two banks.

Josh T. Kohut[1*], Adam B. Kustka[2], Michael Hiscock[3], Phoebe J. Lam[4,5], Chris Measures[6], Allen Milligan[7], Angelicque White[8], Filipa Carvalho[1], Mariko Hatta[6], Bethan M. Jones[2,7], Daniel C. Ohnemus[4,9], John M. Swartz[4,10]

[1]Department of Marine and Coastal Sciences, Rutgers University, New Brunswick, NJ 08901

[2]Department of Earth and Environmental Sciences, Rutgers University, Newark, NJ 07102

[3]US EPA, National Center for Environmental Research, Washington, DC 20460 USA.

[4]Department of Marine Chemistry and Geochemistry, Woods Hole Oceanographic Institution, Woods Hole, MA 02543

[5]now at Department of Ocean Sciences, University of California, Santa Cruz, Santa Cruz, CA 95064

[6]Department of Oceanography, University of Hawaii, Honolulu, HI 96822

[7]Department of Botany and Plant Pathology, Oregon State University, Corvallis, OR 97331,

[8]College of Earth, Ocean and Atmospheric Sciences, Oregon State University, Corvallis, OR 97331

[9]now at Bigelow Laboratory for Ocean Sciences, East Boothbay, ME 04544

[10]now at Institute for Geophysics, Jackson School of Geosciences, The University of Texas at Austin, Austin, Texas 78758

*Author for correspondence email: kohut@marine.rutgers.edu

Keywords: Ross Sea, Phytoplankton, Trace Metals, Mixed Layers, light and iron limitation, bathymetry.

ABSTRACT

Multi-year satellite records indicate an asymmetric spatial pattern in the summer bloom in the Northern Ross Sea, with the largest blooms over the shallows of Pennell Bank compared to Mawson Bank. In 2010-2011, high-resolution spatiotemporal *in situ* sampling focused on these two banks to better understand factors contributing to this pattern. Dissolved and particulate Fe profiles suggested similar surface water depletion of dissolved Fe on both banks. The surface sediments and velocity observations indicate a more energetic water column over Mawson Bank. Consequently, the surface mixed layer over Pennell Bank was more homogeneous and shallower. Over Mawson Bank we observed a thicker more homogeneous bottom boundary layer resulting from stronger tidal and sub-tidal currents. These stronger currents scour the seafloor resulting in sediments less likely to release additional sedimentary iron. Estimates of the quantum yield of photosynthesis and the initial slope of the photosynthesis-irradiance response were lower over Mawson Bank, indicating higher iron stress over Mawson Bank. Overall, the apparent additional sedimentary source of iron to, and longer surface residence time over Pennell Bank, as well as the reduced fluxes from the more isolated bottom mixed layer over Mawson Bank, sustain the observed asymmetric pattern across both banks.

1. Introduction

Phytoplankton blooms in the Ross Sea are extensive (Arrigo & van Dijken, 2004), high productivity events (Arrigo & McClain, 1994) that are responsible for large quantities of carbon export (Asper & Smith, 1999). The Ross Sea continental shelf has the highest rates of net primary productivity in the Southern Ocean? Antarctica (Arrigo et al. 2008a, Smith & Comiso 2008), is a major regional CO_2 sink (Arrigo et al. 2008b) and supports a robust food web containing more than a dozen upper trophic level predators such as penguins, cetaceans and seals (Ballard et al., 2012; Smith et al., 2014). Over continental shelf systems, physical features have suggested that the spatial distribution of phytoplankton blooms and grazers may be linked to local bathymetry and/or tides (Hunt, 1998; Cotté and Simard, 2005, Vlietstra et al., 2005). In the Ross Sea, Reddy and Arrigo (2006) show that the extent of the spring bloom is linked to the underlying bank and trough bathymetry of the outer shelf (Figure 1).

The phytoplankton composition in the Ross Sea has a temporal progression that is potentially driven by varying physical controls on light regime and/or iron supply, although the exact contribution of each factor is debated. In the spring, strong katabatic winds push sea ice offshore and create relatively deep mixed layers. Communities in these waters are often dominated by the haptophyte *Phaeocystis antarctica*, but by early summer the polynya assemblage becomes increasingly dominated by diatoms (Arrigo et al., 1999). The springtime dominance of *P. antarctica* is consistent with its photo-physiology, which is well suited for irradiance conditions resembling those of a deep mixed layer with a dynamic light regime (Kropuenske et al., 2009; Alderkamp et al. 2012). As the season progresses, the water column becomes more stratified, leading to

83 irradiance conditions suitable for diatoms such as *Fragilariopsis cylindricus* (Kropuenske
84 et al., 2009; Alderkamp et al. 2012). Therefore, the spring to summer shifts in
85 community assemblage from *P. antarctica* to diatoms may be related to changes in
86 Mixed Layer Depth (MLD) and light regime. However, concurrent changes in dissolved
87 iron (Fe) potentially confound this relationship. As the polynya first opens, dissolved Fe
88 concentrations in surface waters can be as high as 4 nM (Sedwick et al., 2000). These
89 springtime dissolved Fe concentrations are rapidly drawn down by *P. antarctica* blooms
90 (Sedwick et al., 2011), leading to concentrations that typically remain low throughout the
91 summer. The extent to which these lower Fe concentrations lead to preferential growth
92 of diatoms is not clear. On one hand, some *P. antarctica* populations in the Antarctic
93 Circumpolar Current require higher dissolved Fe concentrations for growth compared to
94 co-occurring diatoms (Coale et al., 2003), and incubation experiments in the Ross Sea
95 have revealed a preferential stimulation of *P. antarctica* by added Fe (Bertrand et al.,
96 2007). However, other field observations and deck incubation results suggest low Fe
97 conditions tend to favor *P. antarctica* over diatoms (Sedwick et al., 2000). Culture
98 experiments demonstrated that species grown under low light have elevated Fe
99 requirements, presumably due to the increased need for Fe-expensive photosynthetic
100 units (Sunda and Huntsman, 1997), which may further complicate our understanding of
101 iron and light limitation in the Southern Ocean.

102 The interplay between micronutrient sources, water column structure, shelf
103 circulation, and local topographic features drives a persistent response in the summer
104 bloom over the northern Ross Sea shelf. This is a critical region for both the exchange of
105 dense bottom water masses that move down the slope and eventually form Antarctic

106 Bottom Water (AABW, Gordon et al., 2009) and the injection of warm Circumpolar
107 Deep Water (CDW) that comes from the mid-depths of the Southern Ocean. The most
108 energetic process that likely contributes to the mixing and advection of these water
109 masses is tides. The tides of the Ross Sea are predominantly diurnal with higher
110 amplitudes over the shallow banks and along the shelf break (Robertson, 2005;
111 Whithworth and Orsi, 2006; Padman et al., 2009). The tides interact with the varying
112 topography and the background flow over the northern Ross Shelf to mix and modify the
113 water masses, likely influencing phytoplankton production in the summer bloom through
114 varying water column stability and delivery of micronutrients to the euphotic zone
115 (Gordon et al., 2009).

116 Using a long-term satellite record, Reddy and Arrigo (2006) describe a persistent
117 spatial pattern in the spring bloom over the Ross Sea Shelf. They show that, on average,
118 the bloom is constrained to the shallows of the banks with much lower biomass levels
119 observed in the basins between the banks. The preferential advection of low biomass
120 water from the north into the basins drives this observed pattern. However, a closer look
121 at the blooms over Pennell and Mawson Banks reveals a persistent asymmetry. The
122 satellite climatology indicates that there is typically more biomass over Pennell Bank
123 (PB) compared to Mawson Bank (MB) and that the largest seasonal blooms occur over
124 PB (Figure 2). Through a multiplatform sampling strategy focused on the two banks, we
125 describe and differentiate the characteristics related to the water column structure over
126 each bank as they relate to the observed asymmetry in the blooms across the banks. We
127 integrate *in situ* physical and biogeochemical measurements sampled across coincident
128 ship and AUV based surveys to determine the conditions that support the observed spatial

pattern across the two banks.

2. Methods

2.1 Satellite derived phytoplankton concentration

NASA Moderate Resolution Imaging Spectroradiometer Aqua (MODIS-A) mapped, monthly, 4.6 km, standard chl *a* estimates (mg m^{-3}) from the 2013 MODIS-A Reprocessing 2013.1 were downloaded from http://oceandata.sci.gsfc.nasa.gov for the months of January and February 2003-2016. Chlorophyll composites were generated for January 1 – February 28 of each year along a 5 pixel wide (~23 km) swath centered on a transect that includes PB and MB (Figures 1 and 2).

2.2 Cruise Transect and Underway Measurements

***2.2.1 Hydrography*:** A ship survey was completed aboard the *RVIB Nathaniel B. Palmer* (NBP). The ship left McMurdo Station on January 19th, 2011 on a 26 day cruise focused primarily on the Northern Shelf across PB and MB (Figure 1). Throughout the cruise, underway measurements of temperature and salinity were taken every second with the NBP thermosalinograph at an intake depth of 6.7 m below the surface. Vertical profiles of velocity were sampled by a ship mounted downward looking 150 KHz Acoustic Doppler Current Profiler (ADCP). These shipboard data were processed with the University of Hawaii Data Acquisition System (UHDAS) software. Raw depth averaged and depth dependent data were detided using the predicted barotropic tide derived from Ross Sea sub-region of the Oregon Tidal Prediction System (Erofeeva et al., 2005).

In addition to the underway data, the ship survey completed 79 stations (Figure 1). Over the course of the cruise the ship made 8 repeat transects across PB and MB (Figure 1). Along this southernmost line that crossed both banks, we sampled 9 stations; 5 over PB, 3 over MB, and one over Joides Basin (JB, Figure 1). At each station there were at least 3 CTD casts with a maximum of 8 casts sampled at the station over the 400 m isobath along the western slope of PB. The Sea-Bird CTD mounted on the rosette was calibrated before and after the cruise. Our analysis will focus on a single along-bank section from off the shelf to the southern end of PB and the 8 repeat cross-sections across PB, JB, and MB (Figure 1).

***2.2.2 Dissolved Trace Metals*:** Samples were collected for dissolved trace metal determinations at 15 of the 79 stations using a custom-built trace metal clean rosette (Measures et al., 2008). Filtered seawater samples (0.45 μm pore size) were determined by shipboard flow injection analysis and duplicate samples were drawn for shore-based determination by Inductively Coupled Plasma Mass Spectrometry (ICP MS; see Hatta et al., this issue for details).

2.2.3 Particulate Trace Metals: Size-fractionated particles (>51 μm, 0.8 - 51 μm) were collected by in-situ filtration using modified dual-flow McLane WTS pumps (Ohnemus and Lam, 2015). The 0.8 - 51 μm size fraction was used to determine the total and leachable concentrations of particulate trace metals using the methods of Ohnemus et al., 2014 and Ohnemus and Lam, 2015 and shore-based High Resolution ICP MS (see Hatta et al., this issue for details).

2.2.4 Surface sediments grain size analysis: Surface sediments were collected using a Smith McIntyre Grab at stations along the southern across-bank section at the 400

175 m isobaths on the western and eastern flanks of PB and MB (stations 71-MB West, 35-
176 MB East, 41-PB West, 28-PB East), at the top of each bank around 280 m depth (stations
177 70-Central MB, 26- Central PB), and at 595 m water depth in the JB in between the two
178 banks (station 34-JB). Additional samples were collected at select stations offshore and
179 inshore of the main section (Figure 1). Sediment subsamples were transferred to 50ml
180 centrifuge tubes and spun down on-board to remove most pore waters, and then frozen
181 for transport.

182 Grain size distributions were determined for surface sediments along the main
183 across-bank section. Sediments were thawed in the laboratory, and subsamples were
184 transferred to a 15mL centrifuge tube and shaken vigorously in water to disperse
185 aggregates, and sieved to remove gravel pieces >2 mm. Grain size distribution for
186 sediments <2 mm was determined on a Beckman Coulter LS13320 Laser Diffraction
187 Particle Size Analyzer at the WHOI Coastal Research Facility. The LS13320 determines
188 the volumetric size distribution from 0.017 μm to 2000 μm. Samples were introduced
189 into the Particle Size Analyzer in an aqueous stream, and sediment concentration was
190 adjusted to reach an obscuration rate between 10-20%. Volume percentages were binned
191 into clay (<4 μm), silt (4-63 μm), and sand (63-2000 μm) size classes (Wentworth, 1922).
192 Broad characteristics of sediment samples off of the main across-bank section were
193 grouped into qualitative sediment classes on the basis of their textural similarities to the
194 sediments for which the grain size distributions were determined (Figure 1).

195 ***2.2.5 Biological sampling*:** Measurements of photosynthetically active radiation
196 (PAR) were taken continuously with a BSI QSR-240 spherical sensor positioned on the
197 mast. Underway parameters, including particulate organic carbon (POC, estimated from

198 beam attenuation) and variable to maximum fluorescence (F_v/F_m), were measured from
199 water collected 6.7 m below the surface, from the ship's underway seawater system.
200 Attenuation and particulate carbon were measured using a Wetlabs hyperspectral
201 absorbance and attenuation (ac-s) meter (as described in Kustka et al., 2015b).

202 ***2.2.6 Productivity:*** Photosynthesis-irradiance experiments were conducted using
203 a ^{14}C-radiotracer method (as described in Kustka et al., 2015b). Primary productivity was
204 calculated by multiplying the percent of carbon labeled by the total carbon available for
205 photosynthesis (e.g. total alkalinity calculated from SST and salinity measured at each
206 station as per Lee et al. (2006) and dividing by incubation time). Rates were also
207 normalized to the concentration chlorophyll a extraction in 90% methanol determined by
208 fluorometry (Strickland and Parsons, 1972).

209 The results of each P–E experiment were fit to a hyperbolic tangent model of
210 Jassby and Platt (1976) using a least-squares non-linear regression in Matlab™ in order
211 to estimate the maximal photosynthetic rate (P^{max} and P_B^{max}) and the light utilization
212 coefficient (α and α_B) with the latter terms calculated after normalization of rates to
213 chlorophyll. The light-saturation index E_K is the quotient of P_B^{MAX} and α_B. Particulate
214 absorption spectra were measured for each incubation as per the quantitative filter pad
215 method described in Mitchell (1990) and Kishino et al. (1985). Briefly, total absorption
216 was measured, methanol was subsequently used to extract pigments from the filtered
217 sample, and detrital absorption was measured. The difference between the two spectra
218 represents lipid-soluble absorption by phytoplankton pigments (a_p (λ)). The mean
219 spectrally weighted $\bar{a}_p$ (m^{-1}) was then calculated as in Hiscock et al., (2008) using the
220 scalar irradiance of the photosynthetron light banks (E(λ)). Photosynthetically usable

221 radiation for each light level was then calculated as PAR multiplied by $\bar{a}_p$. The initial
222 slope of PUR relative to ^{14}C fixation, again determined via least-squares non-linear
223 regression in Matlab™ is an estimate of the quantum yield of carbon uptake (ϕ). All
224 parameters are shown in Table 3. Productivity rates were integrated over the mixed layer
225 using measured P_{max}, α and K_{PAR} values and mean daily integrated surface PAR.

226 ***2.2.7 Phytoplankton Community Composition***: Eukaryotic plankton community
227 structure was investigated using a quantitative high throughput sequence approach
228 targeting the hypervariable V7-9 regions of 18S eukaryotic ribosomal DNA with the
229 Pacific BioSciences SMRT (single molecule real time) sequencing platform. Samples
230 taken from station 7 (Central PB), station 14 (at the shelf break), station 24 (JB), station
231 48 (northern PB) and station 70 (Central MB) were extracted and analyzed. Technical
232 details of sample collection, DNA extraction and subsequent processing, are presented in
233 Jones and Kustka (in review). Sequences were clustered into Operational Taxonomic
234 Units (OTUs) at 98% similarity and the relative abundance of phytoplankton clades were
235 examined in more detail. Dinoflagellates were excluded from further analysis because
236 they are not strictly photosynthetic. It is also worth noting that copy numbers of 18S
237 rDNA are not directly translatable to cell numbers; this is particularly the case for
238 dinoflagellates, where copy numbers can range from hundreds to thousands of copies per
239 cell (Zhu et al. 2005). This means that relatively rare dinoflagellates can result in
240 disproportionate contributions to community structure. While dinoflagellates were
241 present in the unfiltered dataset, there was very scant evidence of this group from
242 shipboard microscopic examinations (Angelicque White, unpub. data).

243 A single sample was collected for each station location, while other samples from

complementary incubation experiments were collected from replicate cubitainers. While we cannot directly report coefficients of variation for these in situ collections, the coefficients of variation for the relative abundances of moderately abundant OTUs (15% or greater) from samples collected from replicate incubation treatments presented in Kustka et al. (2015a) averaged 0.16 (±0.14). This provides an indication of the general reproducibility of community composition relative abundances.

2.3 Autonomous Glider Deployments

Two gliders manufactured by Teledyne Webb Research were deployed during the cruise. The buoyancy-driven propulsion of the glider AUV affords high efficiency and deployment endurance (Schofield et al., 2007). Each glider was equipped with a sensor suite that characterized the ecosystem's physical structure (Conductivity, Temperature, Depth), *in situ* phytoplankton fluorescence and optical backscatter. One glider deployed on February 1, 2011 completed a 9 day mission back and forth across PB. On February 4, 2011 a second shallow glider was deployed near the eastern slope of MB completing a 4-day mission to the west across the bank (Figure 1). The CTD and optical resolution was 0.25m in the vertical and approximately 250m in the horizontal.

2.4 Mixed Layer Depth (MLD) Estimation

For each profile, MLD was determined by finding the depth of the maximum water column buoyancy frequency – max (N^2, Equation 1, Carvalho et al., submitted). For each profile, a quality index (Equation 1) by Lorbacher et al. (2006) was used to quantify the uncertainty in the MLD estimate. Using

267 $$QI = 1 - \frac{rmsd(\rho_k - \overline{\rho})|_{(H_1, H_D)}}{rmsd(\rho_k - \overline{\rho})|_{(H_1, 1.5 \times H_D)}}, \quad (1)$$

268 where ρ_k is the density at a given depth (k) and rmsd( ) denotes the standard deviation
269 from the vertical mean $\overline{\rho}$ from H_1, the first layer near the surface, to a depth D or 1.5xD
270 (where D is the depth of the mixed layer). This index evaluates the certainty in the MLD
271 estimate, where values between 0.8 and 1 represent MLD that were determined with
272 certainty, values between 0.5 and 0.8 represent MLDs determined with uncertainty, and
273 values below 0.5 for MLD estimates that could not be determined. This index does not
274 take into account how strong that inflection is, i.e. how stratified the water column is; just
275 that there is a homogeneous layer present and the MLD calculated is close to the lower
276 boundary of that vertically uniform layer.
277
278 **3. Results**
279 While there is significant year to year variability in chlorophyll across the region,
280 possibly due to differences in physical forcing and timing of sea ice melt, the 14-year
281 satellite time series across PB and MB shows that there has been a persistent pattern
282 across these banks with higher chlorophyll concentration over PB (Figure 2c). Further,
283 the 5 largest blooms in the time series have all occurred over PB, including the 2011
284 bloom sampled during our field season (Figure 2a and b). Over this season, the bloom
285 over PB had chl *a* levels 3 times higher than the observed over MB. The following
286 results focus on this observed asymmetry, consistent with the asymmetry in the spatial
287 pattern over the past 14 years.
288
289

3.1 Physical conditions

Repeated survey transects across PB and MB and the intervening JB highlight the similarities and differences between the oceanographic conditions associated with each bank. Beneath our central transect, MB is characterized as a relatively narrow feature approximately 300 meters deep at its shallowest. Pennell is a much broader and slightly shallower bank with an asymmetric profile. West of the 250 m deep peak, the bank has a much steeper slope than the more gentle slope that lies to the east. Along the western slope of both banks a predominantly barotropic flow delivers deep offshore waters onto the shelf (Figure 3, from Kohut et al., 2013). Differences in the bathymetry of each bank impact the fate of these intrusions as they move south and around the banks (Kohut et al., 2013). Depth averaged currents (Figure 3, black vectors) show that the similarities over each bank are limited to the western slopes. It has been shown that there is a longer pathway for recently introduced MCDW over the western slope of PB onto the bank compared to MB (Kohut et. al., 2013). Additionally, the stronger mean flows over the shallows and eastern slope of MB compared to PB lead to a shorter surface water residence time over MB. The most concentrated MCDW signals are seen near JB and the western slopes of PB and MB (Figure 4, from Kohut et al., 2013). The deep High Salinity Shelf Water (HSSW) is only observed in stations at least 400 m deep. The mean cross section based on all the casts taken at each station shows the significant variation in water column properties across the complicated topography (Figure 4, from Kohut et al., 2013). There is a distinct surface layer of warmer fresher water across the entire section with slightly fresher water over the western slopes of the banks. At depths greater than ~80 m there is significant variability in the distribution of the deeper water masses. In JB

313 there is a thick layer of dense shelf water reaching up from the bottom to a depth of about
314 250 m. Above the western slope of PB, there is a distinct warmer, lower oxygenated
315 MCDW core at depths between 180 and 250 m, centered over the 400 m isobath. While
316 there is evidence of MCDW over the western slope of MB, its potential temperature and
317 oxygen signals are more dilute and spread over a wider range of depths. West of MB the
318 mid water densities consistent with MCDW (Orsi and Wiederwohl, 2009) are distributed
319 more widely throughout the water column. Unlike PB where the MCDW is concentrated
320 over the western slope, the MCDW extends eastward across MB, consistent with other
321 modeling studies (Dinniman et. al., 2003; Dinniman et. al., 2011).

322 The hydrography and chlorophyll fluorescence within the upper 100 m were
323 simultaneously sampled over 2 glider missions, one across each bank (Figure 1 and 5).
324 Over PB, the thermal stratification sampled across the glider section increases in the
325 upper 100 m of the water column proceeding east from JB toward the peak of PB (Figure
326 5, right column). The transect across MB highlights a region of thermally stratified water
327 over the eastern slope punctuated by a well-mixed water column over the shallows of the
328 bank itself (Figure 5, left column). For both banks the highest chlorophyll fluorescence is
329 observed in higher temperatures of the surface waters, just above the stronger thermal
330 stratification. Over PB this occurs over the center of the bank while over MB, the
331 stronger stratification and highest fluorescence is seen over the deeper waters of the
332 eastern slope of the bank. This observed pattern is consistent with both the multi-year
333 satellite record and the 2011 MODIS snapshot taken during our survey (Figure 2).

334 MLDs measured at repeat stations over central PB were persistent over time and
335 were all between 29 and 55 meters (Figure 6). Additionally, the high quality index (QI)

values for 4 of the 5 stations indicate that these MLD estimates are defined with high certainty. Conversely over MB, the QIs for the estimated MLDs were generally lower, with values between 0.40 and 0.84. Two of the 6 repeat stations have QI values below 0.5 indicating that a MLD could not be determined. Almost all of the remaining MLDs were estimated with uncertainty ($0.5 < QI < 0.8$) with the exception of a 76 m deep mixed layer defined with certainty (February 12, Station 78) with QI of 0.84. Additionally the stronger barotropic tides over MB are maintaining a more well-defined and thicker bottom mixed layer over MB, consistent with the velocity dependent vertical height scale of these bottom mixed layers (Simpson and Hunter, 1974). Coincident profiles of Chl-*a* fluorescence at the PB repeat stations correlate well with the estimated MLDs with peak values just above the MLD. The lower Chl-*a* concentrations observed at the MB repeat station were spread more vertically and less correlated with the estimated MLDs when an estimate could be made (Figure 6).

3.2. Dissolved and Particulate metals

The distribution of dissolved Fe (dFe) shows increased concentrations at depth at both MB (up to ~ 0.28 nM) and at repeat stations on PB (~0.22 - 0.36 nM; Figure 7a). Upper water column concentrations were generally low (~0.15 nM) with the exception of two elevated surface water observations for station 61 (discussed below). Total and leachable particulate Fe (pFe) concentrations were uniformly low at the surface (~0.1 nM) and increased strongly with depth at all stations (Figure 7b; Hatta et al., this volume). Near bottom concentrations of total and leachable pFe were highest over MB compared to PB. The proportion of total pFe that was leachable (% leachable pFe) was

359 either constant or decreased with depth.

360

361 ***3.3 Seafloor Sediments***

362 The surface sediment grain size distributions for sediments <2 mm along the main
363 across-bank section are indicated in Table 1. Sediment characteristics followed a similar
364 pattern from west to east across each bank, albeit with different characteristics relative to
365 the topography of each bank. Surface sediments from the western flanks of both MB and
366 PB (MB West, PB West) were characterized by >70% sand, but also contained rocks and
367 abundant gravel pieces >2 mm that were sieved out before being analyzed for grain size
368 distribution (not shown). The sediments at the top of MB (70-Central MB) had abundant
369 consolidated clay and did not have an analogue in any of the sediments sampled on PB.
370 The sediments underlying the higher productivity zones on the eastern flank of MB (35-
371 MB East) and the top of PB (26-Central PB) were both characterized by >70% sand, but
372 less gravel or rocks compared to the sediments on the western flanks. Finally, the
373 sediments to the east of the high productivity regions in the JB (34-TR) and the eastern
374 flank of PB (28-PB East) were characterized by >70% silt (diatom ooze).

375 Sediments off the main across-bank section were not analyzed for particle size
376 distribution, but were classified on the basis of their textural similarities to the sediments
377 on the main section (Figure 1). In general, the sediments in the offshore direction toward
378 the shelf-break were dominated by larger size classes (sand, gravel), whereas the
379 sediments in the inshore direction toward the Antarctic continent were dominated by silt.
380 The general trend observed was thus a progression from a dominance of large to small
381 sediment size classes across the banks from west to east, and along the banks from

382 offshore to inshore.

383 The western flank stations associated with each bank were the locations of the
384 highest depth averaged currents (Figure 3). The wide range in size distribution for
385 sediments at these stations is consistent with strong currents on the western flanks
386 winnowing away fine sediments, exposing the poorly sorted mixture of sediment that
387 reflects the underlying glacial till of the Ross Shelf (Anderson et al., 1984).

388 In contrast, the sediments with high percentage of silt (diatom ooze) indicate
389 relatively quiescent physical conditions that allow for the accumulation of these fine
390 sediments. Indeed, the eastern flank of PB (28-PB East) had the lowest depth averaged
391 currents over the across-bank section (Figure 3). The JB sample was taken close to
392 where the depth-averaged current was zero, shifting from predominantly offshelf to
393 onshelf (Figure 3, Figure 11, Kohut et al., 2013), and its deeper location may function as
394 a local deposition center for winnowed sediments surrounding it.

395

396 ***3.4. Phytoplankton biomass and production***

397 Surface water POC concentrations were elevated along portions of PB, while MB
398 had concentrations lower than PB but slightly greater than along JB (Figure 2b). These
399 features are generally consistent with the multi-season trends in biomass, as
400 approximated by MODIS-derived chlorophyll *a* data (Figure 2). However, while
401 biomass levels were lower on MB, Fv/Fm values obtained at CPB and MB were
402 uniformly low (0.266± 0.027; n=2, and 0.294± 0.024; n= 4, respectively, Table 2). These
403 low values are consistent with Fe-limited growth across the region, corroborated by Fe
404 addition incubations (Kustka et al. 2015a).

405 Biomass normalized maximum productivity values ranged from 1.5 -
406 8.4 g C g chl a^{-1} h^{-1} across the study area, and values for α (the initial slope of the
407 photosynthesis-irradiance curve, [mg C m^{-3} d^{-1} (μmol photons m^{-2} s^{-1})$^{-1}$] ranged from 0.3-
408 5.5 (Table 3) with the highest values measured over PB (station 64, see Fig. 2b). This
409 trend holds for α_B: values ranged from 0.047-0.074 and 0.04-0.12 [g C g chl^{-1} h^{-1}
410 (μmol photons m^{-2} s^{-1})$^{-1}$] over MB and PB, respectively. Similarly, the quantum yield, ϕ,
411 measured in deckboard incubations was also elevated over PB, reaching values of 0.06-
412 0.07 mol C mol photons^{-1} over central PB relative to 0.013-0.022 over MB. Productivity
413 rates integrated over the mixed layer were most pronounced in the PB region (~up to 6.4
414 g C m^{-2} d^{-1}) compared to the lower values observed at MB (~0.6 - 1.1 g C m^{-2} d^{-1}) and
415 other stations (Table 3). We hypothesize that these changes in physiology, e.g. enhanced
416 ϕ, α_B and, α over PB reflect enhanced Fe fluxes to this region relative to MB.
417 The calculated MLD values and the assigned level of confidence around each
418 determined value (expressed as QI, above) help describe the differences in physical
419 regimes on the two banks. However, it is important to point out that we used an accepted
420 but different definition of MLD (one that could not be assigned a QI) to calculate depth
421 integrated productivity in a previous publication (Kustka et al. 2015b) derived from the
422 same dataset. Therefore, the absolute primary productivity numbers will differ, but the
423 trends between the banks and between stations around PB itself are consistent in both
424 analyses.
425
426 ***3.5 Phytoplankton Community Composition***
427 Relative abundances of 18S rDNA corresponding to various genera of

phytoplankton are given in Figure 8. *Fragilariopsis* 18S rDNA abundances were very similar at both station 7 (Central PB) and station 70 (MB; 5 and 6% of the total phototrophs, respectively). Also, the relative abundance of *Phaeocystis* rDNA was also similar and very low at these stations, with abundances less than or equal to 1%, consistent with microscopic observations (unpublished). Two distinct clades of *Chaeotoceros*, referred to as clades 1 and 2, collectively dominated sequences obtained from PB (55%) but had a minor contribution (3.2%) at MB, similar to that observed for the shelf-break station 14. The most striking difference observed between both PB and MB was the dominance of a "*Chaeotoceros*-like" clade, (95% similarity to *Chaetoceros* species within the NCBI-nr database) which comprised 10% and 62% of the sequences obtained from stations 7 and 70, respectively.

4. Discussion

Over the northern Ross Sea Shelf a multi-year satellite record highlights a persistent asymmetric pattern in the distribution of the summer bloom over MB and PB. While there are similarities between both banks, there are critical differences in local physical oceanography and biogeochemistry associated with each bank that support greater phytoplankton biomass over central PB.

The MLDs estimated over central PB were well defined and persistent with an average depth shallower than 40 meters. The relatively weaker mean currents compared to those over MB likely leads to the more persistent, homogeneous and shallower MLDs and longer surface residence times (Figures 3, 5 and 6). Conversely, the narrower MB is characterized by stronger mean currents and less homogeneous surface mixed layers

(Figures 3, 5 and 6). Over central MB there is a strong horizontal shear zone delineating waters to the west where southward transport of offshore waters dominate and those to the east where northward transport of shelf water dominates, suggesting more rapid flushing of surface MB waters. Given the distribution of denser water masses throughout the southwestern Ross Sea (Orsi and Wiederwohl, 2009), this flushing not only reduces surface residence time over the bank, but likely contributes to the deepening of the surface mixed layer. Near the seafloor, the density profiles over MB show a thicker, more homogenous bottom mixed layer that is more distinct from the waters just above. This indicates that the vertical fluxes from this layer may be more inhibited than those observed over PB. This is consistent the theoretical scaling estimates for the vertical height scale of these layers given the stronger tides over MB (Padman et. al., 2003; Padman et. al., 2009; Simpson and Hunter, 1974). These stronger currents are also likely responsible for the more scoured surface sediments observed around and over MB.

The predominance of sandy sediments over MB are not expected to be strong sources of reduced Mn or Fe because of higher oxygen penetration into these porous sediments. The consolidated clays at the top of MB are also not strong sources of reduced Mn or Fe (see Hatta et al., this issue). This can be explained by a smaller accumulation of particulate organic carbon, which supplies the reducing equivalents, to these sediments because of strong scouring, and also because compacted clays have low permeability due to the high tortuosity of clays, potentially impeding diffusion of reduced Mn or Fe from these sediments. The silty sediments found over some stations on PB should be more conducive to dissimilatory reduction of Mn and Fe, since they are composed primarily of diatom ooze and are thus rich in organic carbon, and also have higher permeability than

474 clays, but are not so permeable that oxygen can penetrate. Indeed, bottom concentrations
475 of dissolved Mn were generally higher over PB than MB (Hatta et al., this issue).
476 Further, bottom water concentrations of dissolved Fe over the western flank of PB were
477 higher when the tidal flow was in the offshore direction, pointing to benthic sources of
478 dissolved Fe from silty sediments further inshore (Figure 1). Based on sediment
479 characteristics, PB would be expected to have stronger benthic sources of dissolved Fe.
480 At MB, we observed deeper and more dynamic mixed layers. The deeper more
481 defined bottom layer observed over MB lead to a more isolated bottom mixed layer with
482 stronger currents that scour the seafloor sediments, potentially resulted in lower vertical
483 fluxes of additional iron into the euphotic zone. Lower photosynthetic efficiency
484 (reduced ϕ, α_B) over MB is consistent with reduced Fe fluxes relative to PB. These lower
485 photosynthetic efficiencies are thought to be due to over-production of photosynthetic
486 pigments when phytoplankton are iron stressed; these excess pigments do not contribute
487 to light harvesting (Behrenfeld and Milligan, 2013). Hiscock et al. (2008) similarly relate
488 changes in ϕ and α_B to large changes in Fe availability measured during the Southern
489 Ocean iron enrichment experiment. The light available to populations over each bank is
490 dependent on the depth and consistency of these MLs and the attenuation of light through
491 the surface layer. The higher biomass observed over PB attenuated light such that the
492 median light levels within surface mixed layers over both banks were comparable.
493 The physical and chemical differences between MB and CPB might be
494 expected to influence phytoplankton community composition. For example, the deeper
495 and more dynamic mixed layer might be expected to favor *Phaeocystis antarctica*, based
496 on comparative photo-physiological data between this species and a polar diatom

497 (Alderkamp et al. 2012). However, *P. antarctica* abundances were low on both banks
498 during this study. The two most striking differences in community composition was the
499 dominance of a *Chaetoceros*-like clade at MB (62% at station 70, with modest (~10-
500 15%) contributions at other stations) and the high relative abundances of two
501 *Chaetoceros spp*. clades at PB stations 7 and 48 (combined abundances of 55% and 29%,
502 compared to 3.2% at station 70; Figure 8). The identity or particular physiological
503 characteristics of the *Chaetoceros*-like clade are unknown, but it is intriguing to speculate
504 that this clade is more dominant due to an enhanced ability to flourish under low Fe.
505 Likewise, the higher abundances of the two *Chaetoceros* clades on PB may suggest a
506 lower capacity to deal with lower Fe fluxes. However, complementary 9-day iron
507 incubation experiments did not show any changes in the relative abundances of any of
508 these three clades in response to Fe addition (Kustka et al. 2015b). To better understand
509 the influence of environmental factors on community composition, concurrent collection
510 of unialgal isolates during future campaigns would be instrumental.

511 Based on underway Fv/Fm measurements, both MB and PB populations appear to
512 be growth rate limited by iron availability; this was corroborated by incubation
513 experiments with PB populations (Kustka et al. 2015a). The dissolved Fe profiles were
514 comparable on both banks (Figure 7) with notably similar surface water deficits of
515 dissolved Fe relative to concentrations at depth. The elevated biomass and productivity
516 on PB compared to MB suggests the vertical flux of iron to the surface waters on MB
517 may have been impeded. This is supported by the fundamental differences in the
518 physical structure of the water columns at the two banks, as discussed above.
519

5. Conclusions

The summer bloom over the Northern Ross Sea exhibits a persistent asymmetric spatial distribution with higher biomass over PB compared to MB. Differences in the strength of mean circulation and the tides driven by the local topography of each bank are likely to influence the vertical supply of iron and the residence time of the phytoplankton communities in the surface waters. Stronger tides over MB support a wider and more distinct bottom mixed layer with stronger currents that scour the seafloor. This inhibits the production of sedimentary sources of Fe that could otherwise serve as an iron source to the surface. In the water column, greater exchange with surrounding water masses led to deeper, less defined mixed layers that potentially limit those populations compared to the longer resided and shallow mixed layers observed over PB. Overall the more quiescent conditions observed over and around PB were more conducive to support the higher mid-summer biomass feature repeatedly observed over this bathymetric feature. The water column stability, proximity of silty sediments, and longer residence time maintained by weaker currents of PB leads to the persistent asymmetry in the observed blooms over each bank.

Acknowledgements

The NSF Office of Polar Programs supported the Slocum Enhanced Adaptive Fe Algal Research in the Ross Sea (SEAFAReRS) project (ANT-0839039 to Kohut, Kustka, Milligan, and White; ANT-0839024 to Measures; and ANT-0838921 to Lam). We would also like to thank the entire crew of the *RVIB Nathaniel B. Palmer* for their support throughout the cruise and the Raytheon Polar Services personnel for logistical

assistance. In addition, we are grateful to John Kerfoot (Rutgers) for the glider processing before and after the deployment. This article was prepared while Hiscock was employed at Princeton University. The opinions expressed in this article are the author's own and do not necessarily represent the views or policies of the U.S. Environmental Protection Agency.

References

Anderson, J.B., Brake, C.F., Myers, N.C., 1984. Sedimentation on the Ross Sea continental shelf, Antarctica. Marine Geology 57 (1–4), 295-333. 10.1016/0025-3227(84)90203-2.

Arrigo, K. R., and G. L. Van Dijken. 2004. Annual changes in sea-ice, chlorophyll a, and primary production in the Ross Sea, Antarctica. Deep. Res. Part II Top. Stud. Oceanogr. **51**: 117–138.

Arrigo, K.R. and McClain, C.R., 1994. Spring phytoplankton production in the western Ross Sea. Science: 266: 261-263

Arrigo, K.R., Robinson, D.H., Worthen, D.L., Dunbar, R.B., DiTullio, G.R., VanWoert, M., Lizotte, M.P., 1999. Phytoplankton community structure and the drawdown of nutrients and CO2 in the Southern Ocean. Science 283 (5400), 365-367.

Arrigo, K. R., G. L. van Dijken, and S. Bushinsky. 2008a. Primary production in the Southern Ocean, 1997-2006. J. Geophys. Res. Ocean. **113**: 1997–2006.

Arrigo, K.R., G.L. van Dijken, and M. Long. 2008b. Coastal Southern Ocean: A strong anthropogenic CO2 sink. Geophys. Res. Letters. 35: L21602.

Asper, V., and W. O. Smith Jr. 1999. Particle fluxes during austral spring and summer in southern Ross Sea, Antarctica, J. Geophys. Res., 104, 5345– 5359.

Ballard G, Jongsomjit D, Veloz SD, Ainley DG (2012) Coexistence of mesopredators in an 576 intact polar ocean ecosystem: The basis for defining a Ross Sea marine protected area. Biol 577 Conserv 156:72-82

Behrenfeld, M. J. and Milligan, A. J. (2013) Photophysiological Expressions of Iron Stress in Phytoplankton. Annu. Rev. Mar. Sci., 5, 217-246.

Berger, C.J.M., Lippiatt, S.M., Lawrence, M.G., Bruland, K.W., 2008. Application of a chemical leach technique for estimating labile particulate aluminum, iron, and manganese in the Columbia River plume and coastal waters off Oregon and Washington. J. Geophys. Res. 113, C00B01. 10.1029/2007jc004703.

Bertrand, E. M., M.A. Saito, J. M. Rose, C.R. Riesselman, M.C. Lohan, 2007. A.E. Noble, P.A. Lee, and G.R. DiTullio, Vitamin B12 and iron colimitation of phytoplankton growth in the Ross Sea., Limnol. Oceanogra. , 52, 1079-1093, doi:10.4319/lo.2007.52.3.1079.

Carvalho, F., Schofield, O., Oliver, M., Kohut, J. 2016. Mixing and phytoplankton dynamics in Antarctica's Coastal Seas. (In Prep).

Coale, K. H., X. J. Wang, S. J. Tanner, and K. S. Johnson. 2003. Phytoplankton growth and biological response to iron and zinc addition in the Ross Sea and Antarctic Circumpolar Current along 170°W. Deep Sea Research Part II 50:635–653, doi:10.1016/ S0967-0645(02)00588-X.

Cotté C, Simard Y. 2005. Formation of dense krill patches under tidal forcing at whale feeding hot spots in the St. Lawrence Estuary. *Marine Ecology Progress Series* 288: 199–210. doi: 10.3354/meps288199.

Dinniman, M. S., Klinck, J. M., & Smith, W. O. 2003. Cross-shelf exchange in a model of the Ross Sea circulation and biogeochemistry. Deep Sea Research Part II: Topical Studies in Oceanography, 50(22-26), 3103-3120. doi: 10.1016/j.dsr2.2003.07.011

610 Dinniman, M. S., Klinck, J. M., & Smith, W. O. 2011. A model study of Circumpolar
611 Deep Water on the West Antarctic Peninsula and Ross Sea continental shelves.
612 *Deep Sea Research Part II: Topical Studies in Oceanography*, *58*(13),
613 1508-1523.
614 Erofeeva, S. Y., L. Padman and G. Egbert. 2005. Assimilation of Ship-Mounted ADCP Data for
615 Barotropic Tides: Application to the Ross Sea. Journal of Atmospheric and Oceanic
616 Technology 22(6): 721-734.
617 Gordon, A. L., L. Padman and A. Bergamasco. 2009. Southern Ocean shelf slope exchange.
618 Deep Sea Research Part II: Topical Studies in Oceanography 56(13-14): 775-777.
619 Hatta et al., this volume The relative roles of Modified Circumpolar Deep Water and
620 sediment resuspension in maintaining the phytoplankton blooms above Pennell
621 and Mawson Bank, Ross Sea.
622 Hiscock, M.R., Lance, V.P., Apprill, A., Bidigare, Johnson, Z.I., R.R., Mitchell, B.G., Smith,
623 Jr., W. O., Barber, R.T., 2008. Photosynthetic maximum quantum yield increases are
624 an essential component of the Southern Ocean phytoplankton response to iron.
625 Proceedings of the National Academy of Science, 105, 4775-4780.
626 Hunt Jr G. L., Russell R. W., Coyle K. O., Weingartner T. 1998. Comparative foraging
627 ecology of planktivorous auklets in relation to ocean physics and prey availability.
628 *Marine Ecology Progress Series* 167: 241–259. doi: 10.3354/meps167241
629 Jones, B.M., and Kustka, A.B. (Submitted) Quantitative SMRT cell sequencing unveils
630 differential distribution of protists in the Ross Sea, Antarctica. *Marine*
631 *Biotechnology*
632 Kishino, M., Takahashi, M., Okami, N., Ichimura, S., 1985. Estimation of the spectral
633 absorption coefficients of phytoplankton in the sea. Bull. Mar. Sci. 37 (2),
634 634-642.
635 Kohut, J., Hunter, E., Huber, B., 2013. Small-scale variability of the cross-shelf flow over
636 the outer shelf of the Ross Sea. Journal of Geophysical Research: Oceans 118 (4),
637 1863-1876. 10.1002/jgrc.20090.
638 Kropuenske, L.R.,Mills,M.M.,VanDijken,G.L.,Bailey,S.,Robinson,D.H.,Welsch- meyer,
639 N.A.,Arrigo,K.R. 2009. Photophysiology in two major Southern Ocean
640 phytoplankton taxa: photoprotectionin Phaeocystis antarctica and Fragilar-iopsis
641 cylindrus. Limnol.Oceanogr. 54(4),1176–1196.
642 Kustka, A., Jones, B.M., Hatta, M., Field, M. P., and A. J. Milligan, 2015a. The influence
643 of iron and siderophores on eukaryotic phytoplankton growth rates and
644 community composition in the Ross Sea, Marine Chemistry. 173. 195-207.
645 doi:10.1016/j.marchem.2014.12.002.
646 Kustka, A.B., J.T. Kohut, A. White, P.J. Lam, A. Milligan, M. Dinniman, S. Mack, M.
647 Hiscock, E. Hunter, W.O. Smith, Jr., and C.I. Measures. 2015b. The role of
648 Modified Circumpolar Deep Water as an iron source to productive mid-
649 summer phytoplankton in the Ross Sea. Deep Sea Res. 105:171-185.
650 Lee, K., Tong, L.T., Millero, F.J., Sabine, C.L., Dickson, A.G., Goyet, C., Park, G.-H.,
651 Wanninkhof, R., Feely, R.A., Key, R.M., 2006. Global relationships of total
652 alkalinity with salinity and temperature in surface waters of the world's oceans.
653 Geophys.Res.Lett.33, L19605.

Lorbacher, K., D. Dommenget, P. Niiler, and A. Köhl. 2006. Ocean mixed layer depth: A subsurface proxy of ocean-atmosphere variability, Journal of Geophysical Research: Oceans (1978–2012), 111(C7).

Measures, C. I., W. M. Landing, M. T. Brown, and C. S. Buck. 2008. A commercially a vailable rosette system for trace metal clean sampling, *Limnol. Oceanogr. Methods* 6:384-394. doi: 10.4319/lom.2008.6.384.

Measures, C.I., J. Yang, and J.A. Resing, J. 1995. Determination of iron in seawater by flow injection analysis using in-line preconcention and spectrophotometric detection, Mar. Chem., 50, 3-12, 1995.

Milne, A., Landing, W., Bizimis, M., Morton, P. 2010. Determination of Mn, Fe, Co, Ni, Cu, Zn, Cd and Pb in seawater using high resolution magnetic sector inductively coupled mass spectrometry (HR-ICP-MS). Anal. Chim. Acta. 665, 200–207.

Mitchell, B.G., 1990. Algorithms for determining the absorption coefficient of aquatic particulates using the Quantitative Filter Technique (QFT). Society of Photo-Optical Instrumentation Engineers 10, 137-148.

Ohnemus, D.C., Auro, M.E., Sherrell, R.M., Lagerstrom, M., Morton, P.L., Twining, B.S., Rauschenberg, S., Lam, P.J., 2014. Laboratory intercomparison of marine particulate digestions including Piranha: a novel chemical method for dissolution of polyethersulfone filters. Limnology and Oceanography-Methods 12, 530-547. 10.4319/lom.2014.12.530.

Ohnemus, D.C., Lam, P.J., 2015. Cycling of lithogenic marine particles in the US GEOTRACES North Atlantic transect. Deep Sea Research Part II: Topical Studies in Oceanography 116, 283-302. http://dx.doi.org/10.1016/j.dsr2.2014.11.019.

Orsi, A. H. and C. L. Wiederwohl (2009). A recount of Ross Sea waters. Deep Sea Research Part II: Topical Studies in Oceanography. 56(13-14): 778-795.

Padman, L., Erofeeva, S., and Joughin, I. 2003. Tides of the Ross Sea and Ross Ice Shelf cavity. *Antarctic Science* 15.01:31-40.

Padman, L., Howard, S., Orsi, A., Muench, R., 2009. Tides of the Northwestern Ross Sea and their impact on dense outflows of high salinity shelf water. In: Gordon, A., Padman, L., Bergamasco, A. (Eds.), Deep-Sea Research AnSlope/Clima topical volume. Southern Ocean Shelf Slope Exchange.

Raiswell, R., Canfield, D.E., Berner, R.A., 1994. A comparison of iron extraction methods for the determination of degree of pyritisation and the recognition of iron-limited pyrite formation. Chemical Geology 111 (1-4), 101-110.

Robertson, R. 2005. Baroclinic and barotropic tides in the Ross Sea. Antarctic Science, 17(1), 107-120. doi: 10.1017/s0954102005002506

Schofield, O., Kohut, J., Aragon , D., Creed, L., Graver, J., Haldeman, C., Kerfoot, J., Roarty, H., Jones, C., Webb, D., Glenn, S. M (2007). Slocum Gliders: Robust and ready. Journal of Field Robotics, 24(6): 1-14, doi: 10:1009/rob.20200.

Simpson, J.H., and Hunter, J.H. 1974. Fronts in the Irish Sea. Nature, 250, 404-406. doi:10.1038/250404a0.

Sedwick, P.N., DiTullio, G.R., Mackey, D.J., 2000. Iron and manganese in the Ross Sea, Antarctica: Seasonal iron limitation in Antarctic shelf waters. Journal of Geophysical Research-Oceans 105 (C5), 11321-11336.

Sedwick, P. N., C.M. Marsay, B.M. Sohst, A.M. Aguilar-Islas, M.C. Lohan, M.C. Long, K.R. Arrigo, R.B. Dunbar, M.A. Saito, W.O. Smith, G.R. DiTullio, 2011. Early season depletion of dissolved iron in the Ross Sea polynya: Implications for iron dynamics on the Antarctic continental shelf, J. Geophys. Res., 116, C12019, doi:10.1029/2010JC006553.

Smith, W.O., Comiso, J.C., 2008. Influence of sea ice on primary production in the Southern Ocean: a satellite perspective. J.Geophys.Res.113,1–19.

Smith, W.O., David G. Ainley, Kevin R. Arrigo, and Michael S. Dinniman. 2014. The Oceanography and Ecology of the Ross Sea. Annu. Rev. Mar. Sci. 6:469–87

Strickland, J.D.H., and Parsons, T.R. 1972. A practical handbook of seawater analysis. Fisheries Res. Board of Canada, Ottowa, 310 pp.

Sunda, W.G. and S. Huntsman. 1997. Interrelated influence of iron, light and cell size on marine phytoplankton growth. Nature 390:389-392.

Vlietstra L. S., Coyle K. O., Kachel N. B., Hunt Jr G. L. 2005 Tidal front affects the size of prey used by a top marine predator, the short-tailed shearwater (*Puffinus tenuirostris*). *Fisheries Oceanography* 14: 196–211. doi: 10.1111/j.1365-2419.2005.00369.x

Wentworth, C.K., 1922. A scale of grade and class terms for clastic sediments. The Journal of Geology, 377-392.

Whitworth, T. and A. H. Orsi (2006). Antarctic Bottom Water production and export by tides in the Ross Sea. Geophysical Research Letters. 33(12).

Zhu, F., R. Massana, F. Not, D. Marie, And D. Vaulot. 2005. Mapping Of Picoeucaryotes In Marine Ecosystems With Quantitative PCR Of The 18s Rrna Gene. Fems Microbiology Ecology 52: 79-92.

List of Tables and Figures

Table 1: Surface sediment grain size classification (volume %). Station abbreviations are Mawson Bank West (MW), Central Mawson Bank (MT), Mawson Bank East (ME), Joides Basin (JB), Pennell Bank West (PW), Central Pennell Bank (PT), and Pennell Bank East (PE). *Wentworth sediment classes are defined as: silty sand=sand>silt>10%; sandy silt=silt>sand>10%; clayey silt=silt>clay>10% (Wentworth, 1922). All other classes <10%.

Table 2. Underway variable fluorescence from select stations. Average values from 60 observations (within 30 minutes preceding and following station arrival time) are reported. Locations refer to Central Pennell Bank and Mawson Bank, respectively. Time of sampling is listed as Julian day relative to GMT. Irradiance (mast PAR) is expressed in umol photon m^{-2} s^{-1}. Fv/Fm was measured using a Satlantic FIRE fluorometer as described in text. For calculations of location Fv/Fm, observations where mast PAR exceeded 300 μmol photon m^{-2} s^{-1} were omitted (corresponding to ~ 100 μmol photon m^{-2} s^{-1} at the collection depth) due to potential non-photochemical quenching.

Table 3. Primary productivity rates as well as parameters of hyperbolic tangent model for 24-hr 14C incubations. Error terms are the confidence intervals of the model fit. Maximal productivity rates are shown as calculated with and without normalization to chlorophyll. The quantum yield is calculated as denoted in the text; the half saturation coefficient (Ek) is determined from Pmax and alpha. The location of each station relative to the longitudinal bank topography is noted as EF (Eastern Flank), CB (Central Bank), NB (Northern Bank), or WF (Western Flank).

Figure 1. Map of the study site in the Western Ross Sea showing the ship track (black line), ship stations (black dots), and glider tracks (green). Isobaths highlight the relevant topographic features including Ross Bank (RB), Pennell Bank (PB), Joides Basin (JB), and Mawson Bank (MB). The colored circles indicate the broad sediment characteristics of surface sediments. The repeat ship section is the southern most line across the two banks coincident with the glider deployments.

Figure 2. Historical and 2011 mid-summer biomass proxies across transect spanning Pennell and Mawson Banks. a) MODIS-derived Chl a concentration (ug/L) during our survey in January 2011. Our primary sampling transect across the banks is shown in white. b) Underway estimates of particulate organic carbon from hyperspectral absorbance and attenuation. c) January through February mean satellite derived Chl a concentration along our sampling line. Years 2003-2016 are grey and 2011 is blue. d) Bathymetric profile highlighting Pennell Bank (PB) and Mawson Bank (MB) relative to the seasonal Chl-a concentrations shown above in panel c.

779 Figure 3. Velocity characteristics across transect spanning PB and MB a) detided depth
780 averaged currents (black vectors) and surface temperature (colored track). The depth
781 dependent velocity sections (m/s) for the cross bank (b) and along bank (c) velocity
782 components. These are the average of cross-sections sampled between Jan 22 and Feb 12,
783 2011. The relevant topographic features including Pennell Bank (PB), Joides Basin (JB),
784 and Mawson Bank (MB) are also labeled.
785
786 Figure 4. Average cross section of potential temperature (°C, top), salinity (psu,
787 middle) and dissolved oxygen (ml L^{-1}, bottom). The stations sampled as part of the
788 across bank section are shown as vertical dashed lines. The neutral density bounds
789 defining MCDW (28.00-28.27 kg m^{-3}) are shown in black and the topographic features
790 are labeled as in Figure 1.
791
792 Figure 5. Glider cross-sections of Temperature (top row), Chlorophyll Concentration
793 determined from fluorescence (middle row), and the underlying bathymetry of each bank
794 (bottom row). The deployment over PB is the right column and the deployment over the
795 narrower MB is the left column. The distance along track is referenced to the profile
796 closest to JB and increases as the glider moves away from JB. The tracks are shown as
797 green lines in Figure 1.

798
799 Figure 6: Shipboard profiles of Density (dashed blue) and Chl a Fluorescence (green) for
800 the central PB (upper row) and central MB (lower row) Stations. The estimated MLD is
801 shown as a solid red line for each station. The date, station number, MLD, quality index
802 (QI), and daily mean wind velocity are indicated for each profile. The average MLD and
803 MLD integrated Chl a fluorescence for each bank is also shown.

804
805 Figure 7: The vertical depth (m) profiles of (a) dissolved Fe (dFe, nM) and (b) leachable
806 particulate Fe (pFe, nM) for the repeated stations above PB (Stations 7-red circles and
807 61-green squares) and above MB (Station 70-purple diamonds).
808
809 Figure 8. Relative abundances of 18S rDNA from phytoplankton genera at PB (7), off the
810 shelf (14), PB West (24), PB North (48) and MB (70). Operationally defined taxonomic
811 units (OTUs) were clustered at 98% sequence similarity. For clarity, only OTUs
812 representing at least 1% of phototroph OTUs are shown, so some treatments have
813 summed relative abundances less than 100%. For station 7 (PB), the relative abundances
814 of four relatively rare diatom OTUs (with similarity to *Proboscia* spp., *Thalassiosira*
815 spp., *Thalassiothrix* spp., and *Pleurosigma* spp.) are pooled as, "four other diatom
816 clades". Assemblage data were derived from single samples collected from the mixed
817 layer at each station.

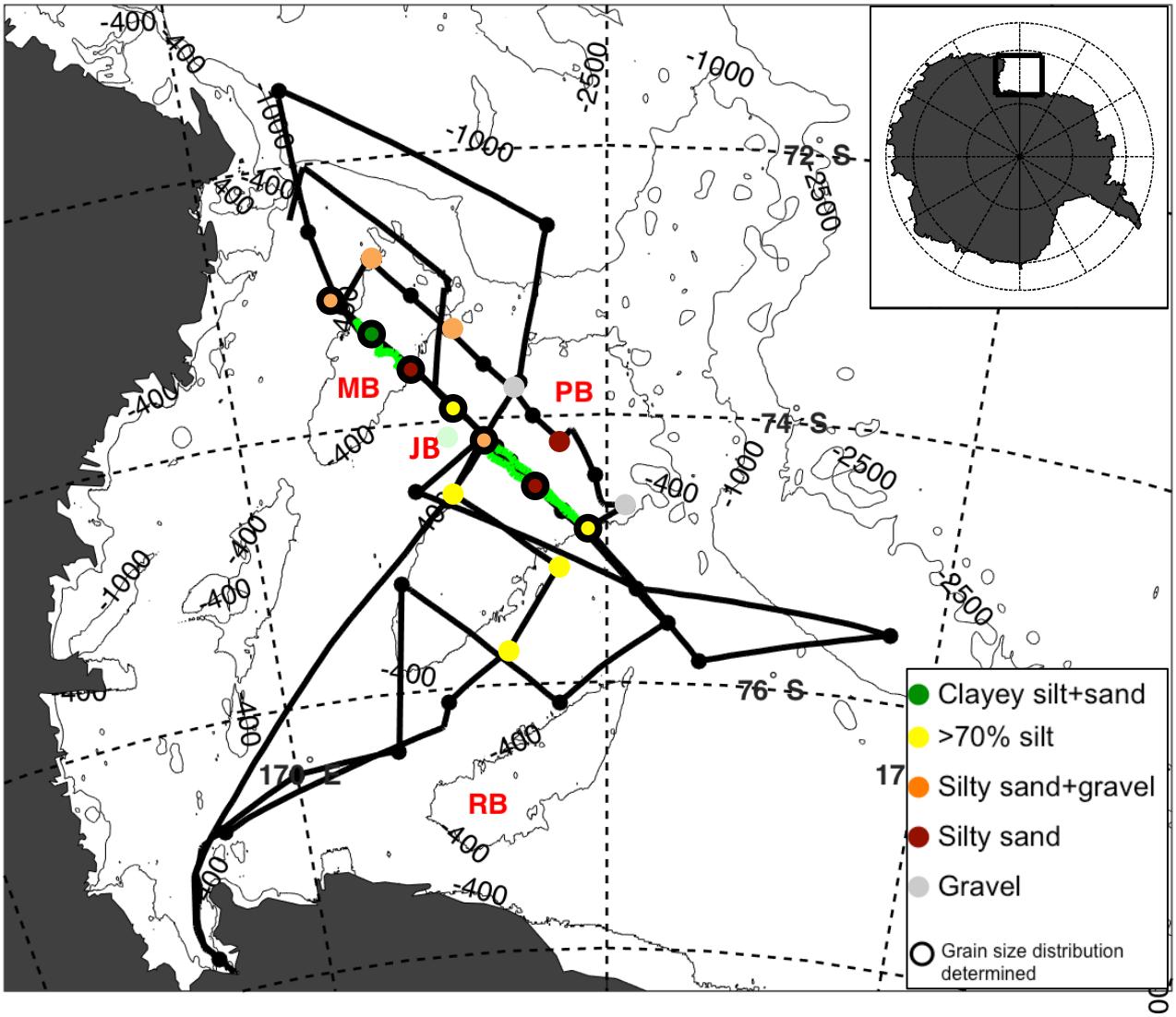

Figure 1. Map of the study site in the Western Ross Sea showing the ship track (black line), ship stations (black dots), and glider tracks (green). Isobaths highlight the relevant topographic features including Ross Bank (RB), Pennell Bank (PB), Joides Basin (JB), and Mawson Bank (MB). The colored circles indicate the broad sediment characteristics of surface sediments. The repeat ship section is the southern most line across the two banks coincident with the glider deployments.

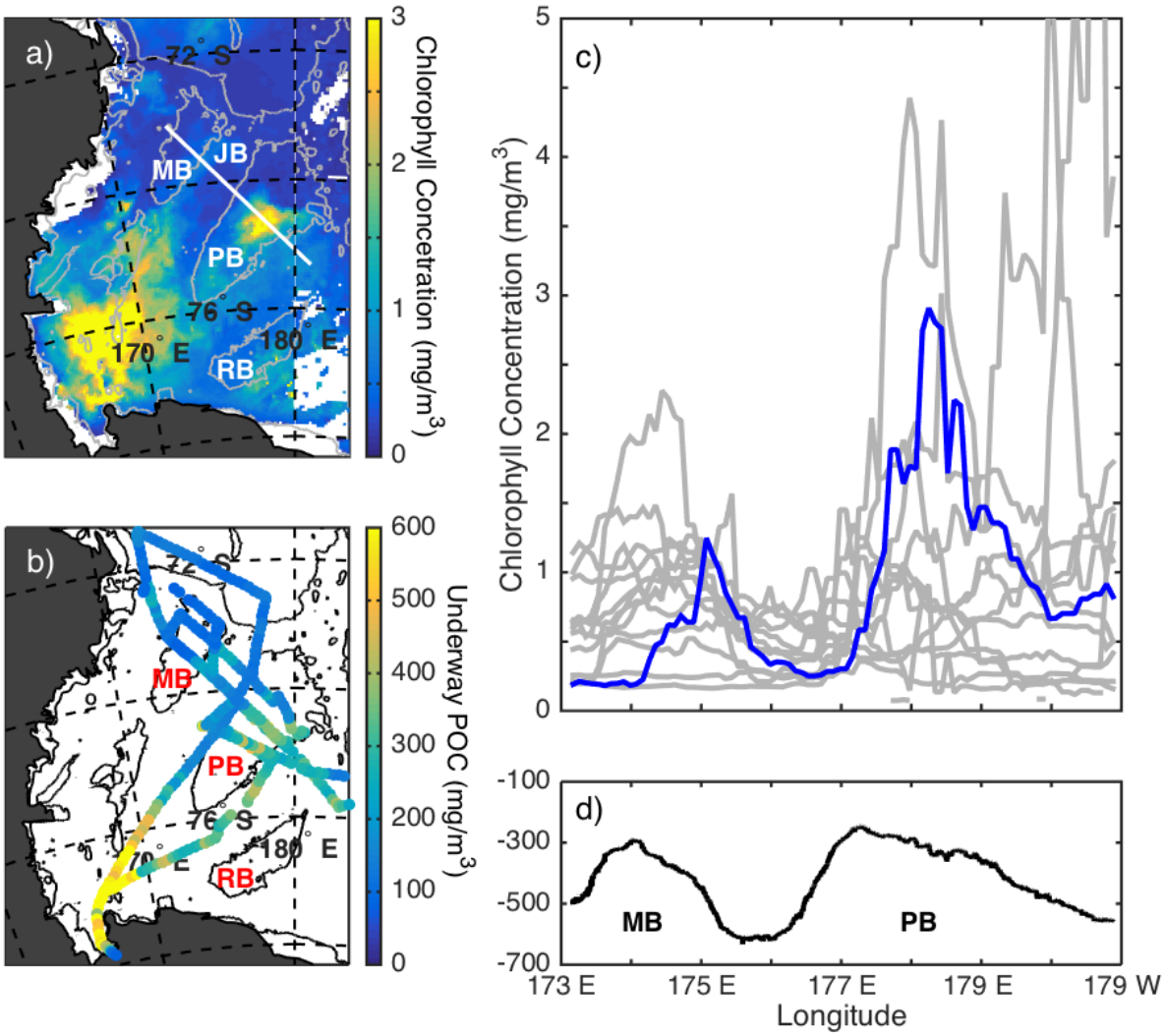

Figure 2. Historical and 2011 mid-summer biomass proxies across transect spanning Pennell and Mawson Banks. a) MODIS-derived Chl a concentration (ug/L) during our survey in January 2011. Our primary sampling transect across the banks is shown in white. b) Underway estimates of particulate organic carbon from hyperspectral absorbance and attenuation. c) January through February mean satellite derived Chl a concentration along our sampling line. Years 2003-2016 are grey and 2011 is blue. d) Bathymetric profile in meters highlighting Pennell Bank (PB) and Mawson Bank (MB) relative to the seasonal Chl-a concentrations shown above in panel c.

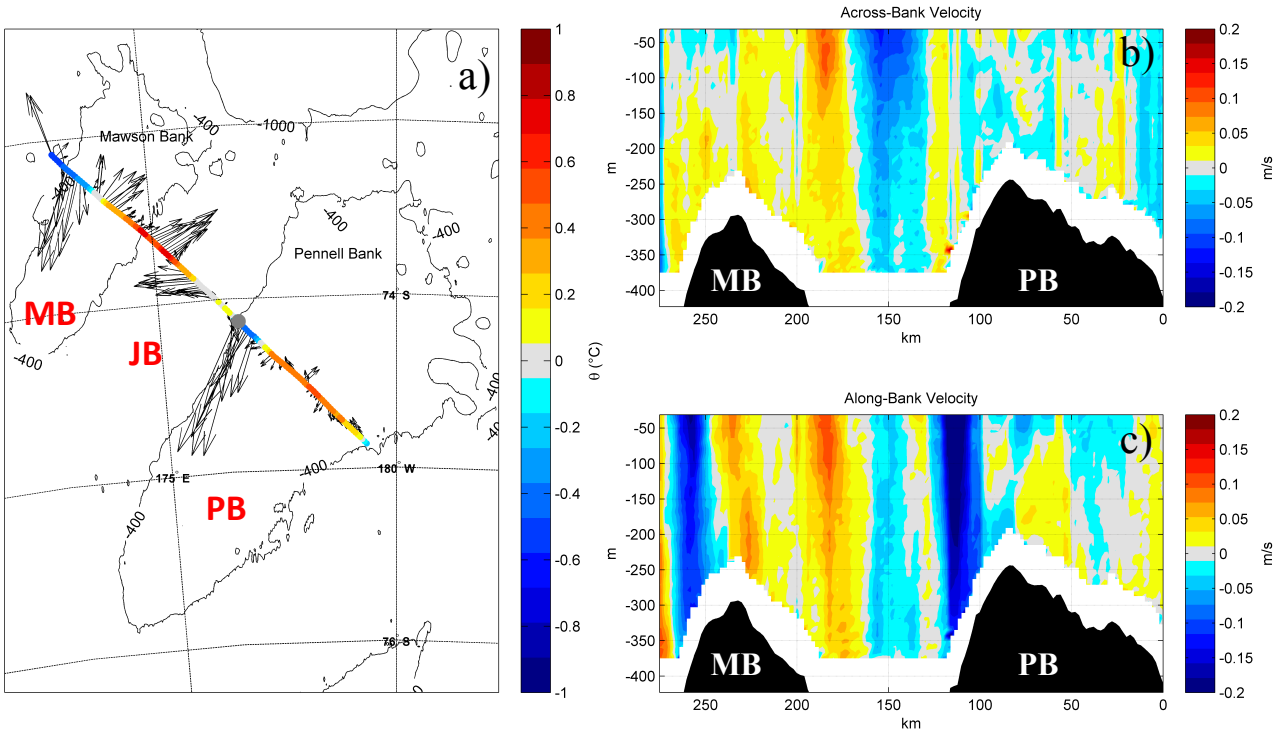

Figure 3. Velocity characteristics across transect spanning PB and MB a) detided depth averaged currents (black vectors) and surface temperature (colored track). The depth dependent velocity sections (m/s) for the cross bank (b) and along bank (c) velocity components. These are the average of cross-sections sampled between Jan 22 and Feb 12, 2011. The relevant topographic features including Pennell Bank (PB), Joides Basin (JB), and Mawson Bank (MB) are also labeled.

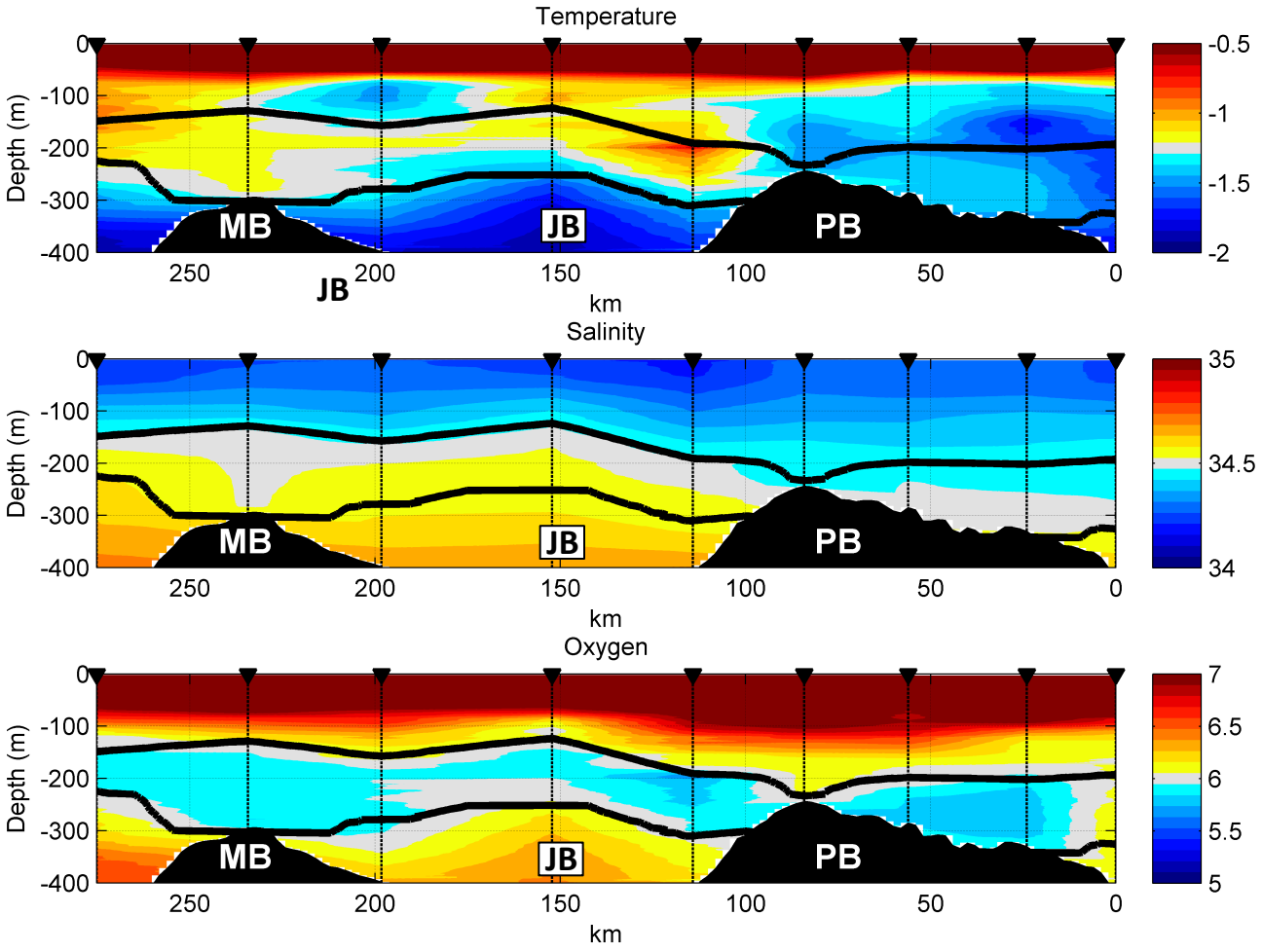

Figure 4. Average cross section of potential temperature (°C, top), salinity (psu, middle) and dissolved oxygen (ml L^{-1}, bottom). The stations sampled as part of the across bank section are shown as vertical dashed lines. The neutral density bounds defining MCDW (28.00-28.27 kg m^{-3}) are shown in black and the topographic features are labeled as in Figure 1.

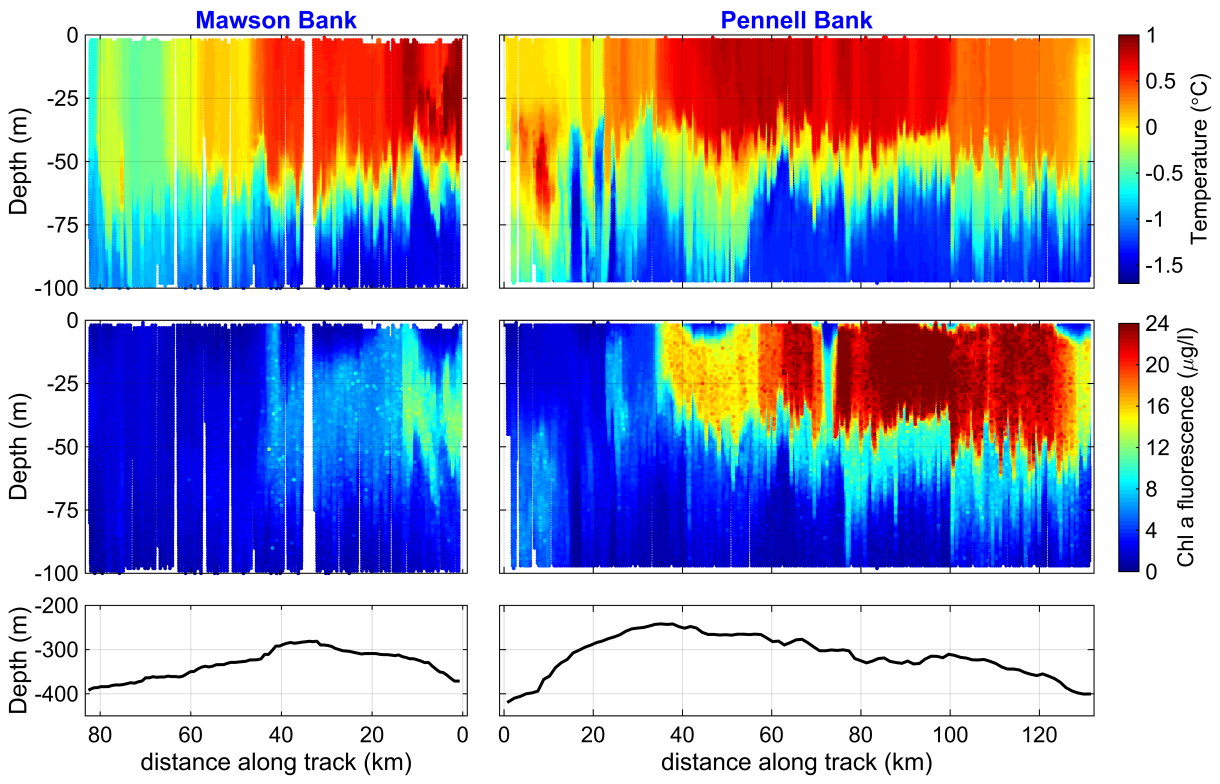

Figure 5. Glider cross-sections of Temperature (top row), Chlorophyll Concentration determined from fluorescence (middle row), and the underlying bathymetry of each bank (bottom row). The deployment over PB is the right column and the deployment over the narrower MB is the left column. The distance along track is referenced to the profile closest to JB and increases as the glider moves away from JB. The tracks are shown as green lines in Figure 1.

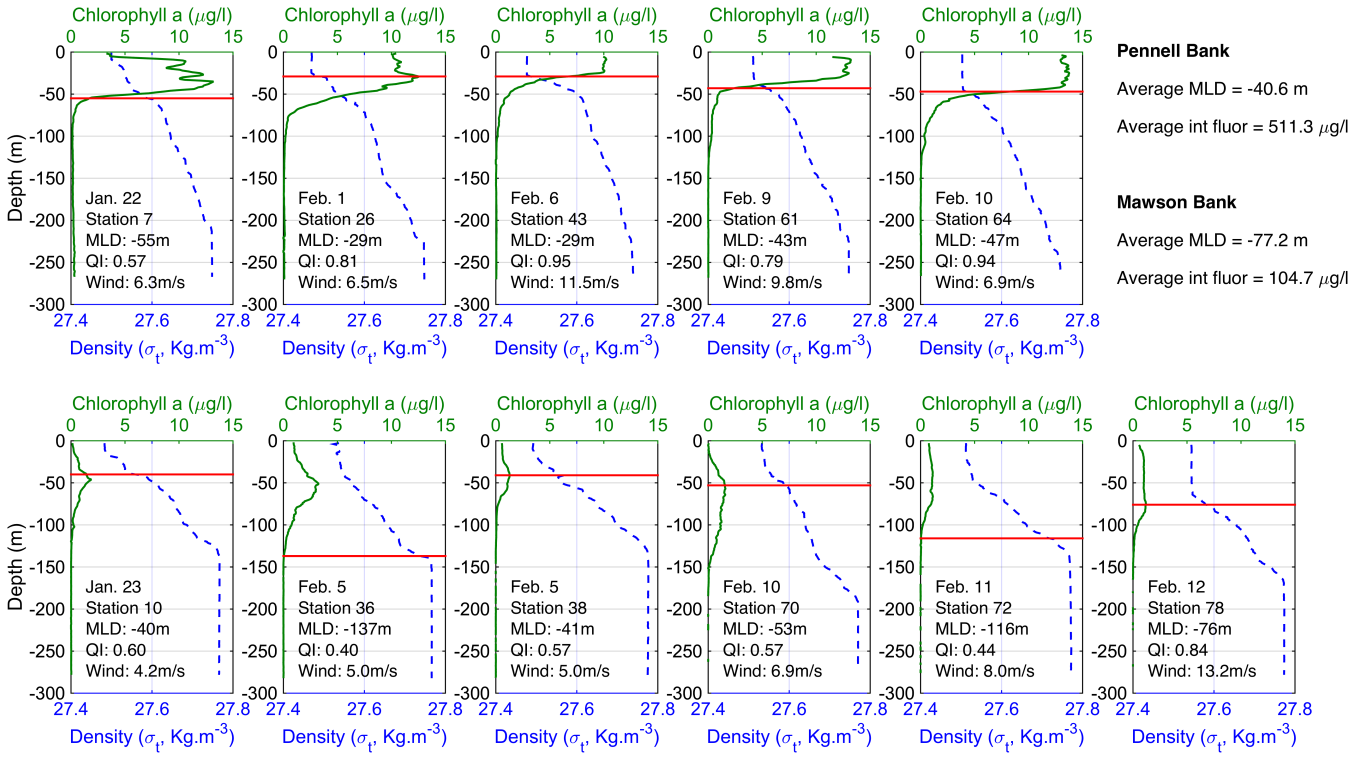

Figure 6: Shipboard profiles of Density (dashed blue) and Chl a Fluorescence (green) for the central PB (upper row) and central MB (lower row) Stations. The estimated MLD is shown as a solid red line for each station. The date, station number, MLD, quality index (QI), and daily mean wind velocity are indicated for each profile. The average MLD and MLD integrated Chl a fluorescence for each bank is also shown.

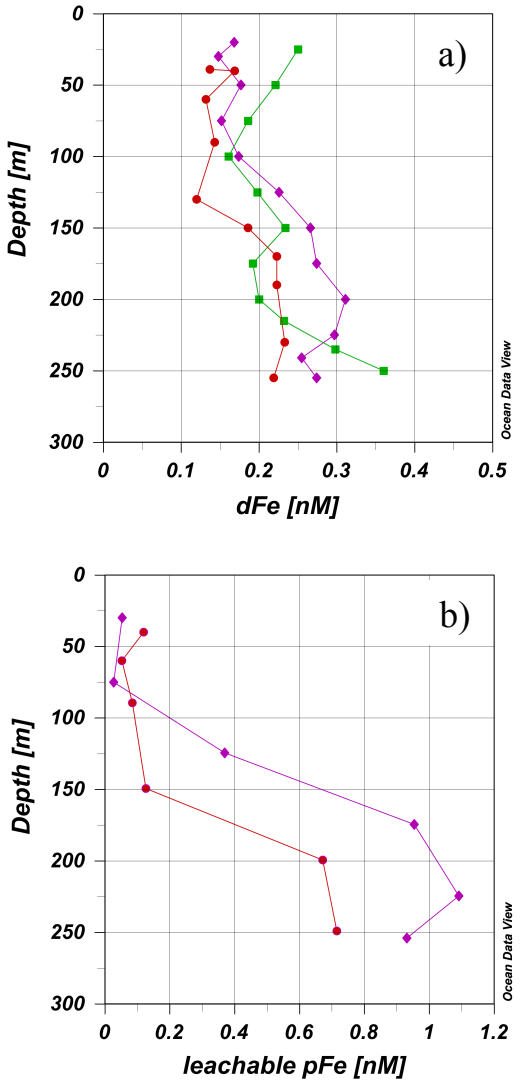

Figure 7: The vertical depth (m) profiles of (a) dissolved Fe (dFe, nM) and (b) leachable particulate Fe (pFe, nM) for the repeated stations above PB (Stations 7-red circles and 61-green squares) and above MB (Station 70-purple diamonds).

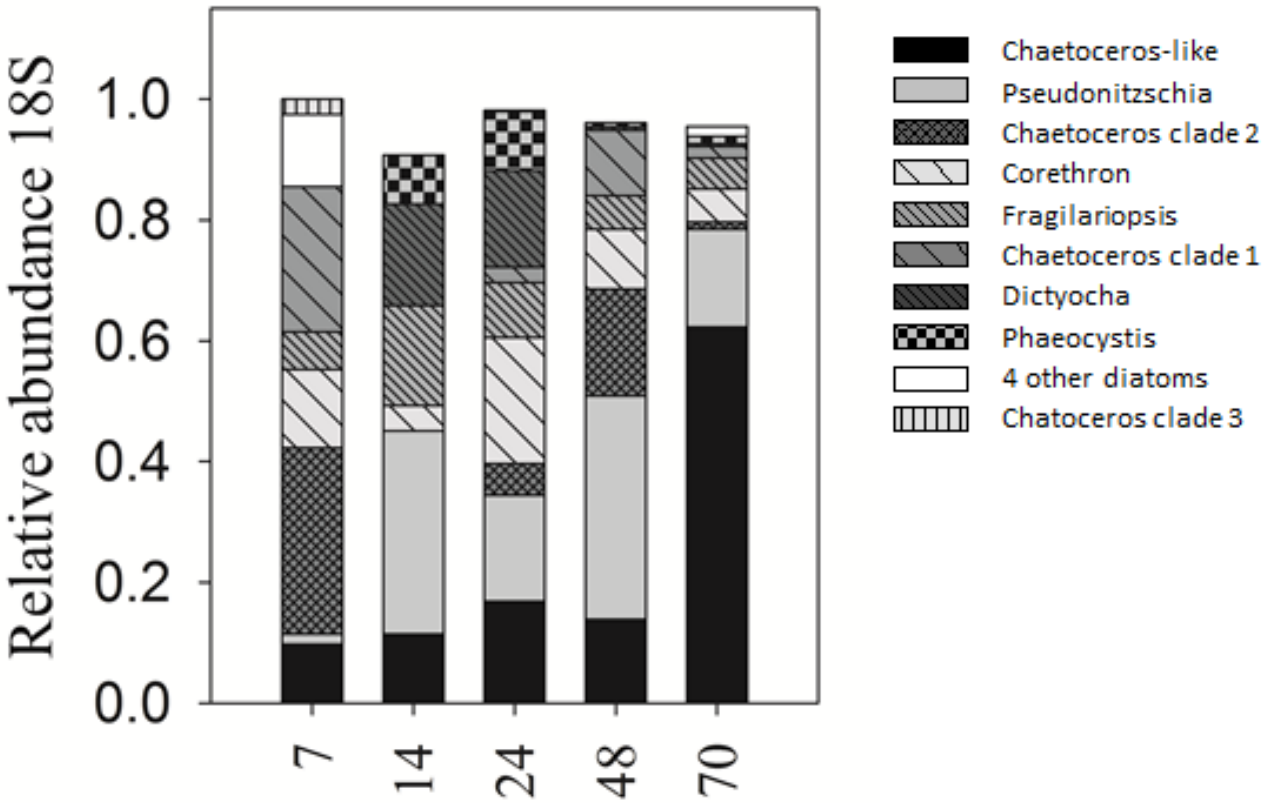

Figure 8. Relative abundances of 18S rDNA from phytoplankton genera at PB (7), off the shelf (14), PB West (24), PB North (48) and MB (70). Operationally defined taxonomic units (OTUs) were clustered at 98% sequence similarity. For clarity, only OTUs representing at least 1% of phototroph OTUs are shown, so some treatments have summed relative abundances less than 100%. For station 7 (PB), the relative abundances of four relatively rare diatom OTUs (with similarity to *Proboscia* spp., *Thalassiosira* spp., *Thalassiothrix* spp., and *Pleurosigma* spp.) are pooled as, "four other diatom clades". Assemblage data were derived from single samples collected from the mixed layer at each station.

Table 1: Surface sediment grain size classification (volume %)

Station #	71-MW	70-MT	35-ME	34-JB	41-PW	26-PT	28-PE
Clay: <4um	5	27	3	13	3	2	9
Silt: 4-63um	22	53	12	79	12	14	73
sand: 63um-2mm	73	20	85	8	86	84	17
Wentworth sediment class*	silty sand +gravel	clayey silt +sand (>10%)	silty sand	clayey silt	silty sand +gravel	silty sand	sandy silt

Station abbreviations are Mawson Bank West (MW), Central Mawson Bank (MT), Mawson Bank East (ME), Joides Basin (JB), Pennell Bank West (PW), Central Pennell Bank (PT), and Pennell Bank East (PE)

*Wentworth sediment classes are defined as: silty sand=sand>silt>10%; sandy silt=silt>sand>10%; clayey silt=silt>clay>10% (Wentworth, 1922). All other classes <10%.

Table 2. Underway variable fluorescence from select stations.

Station	Location	Julian day (GMT)	PAR	Fv/Fm (sd)
26	Central PB	32.50	30	0.247 (0.014)
43	Central PB	37.57	13	0.285 (0.017)
61	Central PB	40.92	891	0.277 (0.017)
64	Central PB	41.28	584	0.265 (0.022)
36	Central MB	36.42	42	0.313 (0.016)
38	Central MB	36.66	48	0.315 (0.029)
70	Central MB	41.96	1593	0.191 (0.021)
72	Central MB	42.56	5	0.281 (0.034)
78	Central MB	43.86	298	0.267 (0.036)

Average values from 60 observations (within 30 minutes preceding and following station arrival time) are reported. Locations refer to Central Pennell Bank and Mawson Bank, respectively. Time of sampling is listed as Julian day relative to GMT. Irradiance (mast PAR) is expressed in umol photon m^{-2} s^{-1}. Fv/Fm was measured using a Satlantic FIRE fluorometer as described in text. For calculations of location Fv/Fm, observations where mast PAR exceeded 300 µmol photon m^{-2} s^{-1} were omitted (corresponding to ~ 100 µmol photon m^{-2} s^{-1} at the collection depth) due to potential non-photochemical quenching.

Table 3. Primary productivity rates as well as parameters of hyperbolic tangent model for 24-hr 14C incubations.

Date (2011)	Sta.	**Mixed Layer Integrated NPP** g C m^{-2} d^{-1}	**P_{max}** mg C m^{-3} d^{-1}	**α**, mg C m^{-3} d^{-1} μmol photons m^{-2} s^{-1}	**P_b^{max}** g C g chl^{-1} h^{-1}	**α**, g C g chl a^{-1} $^{h-1}$ μmol photons m^{-2} s^{-1}	**Quantum Yield** mol C mol photons $^{-1}$	**E_k** μmol m^{-2} s^{-1}
Mawson Bank								
24-Jan	11, EF	1.14	38 ± 3	0.4 ± 0.1	4.3 ± 0.4	0.047 ± 0.010	0.013 ± 0.003	93.2
11-Feb	70, C	0.60	12 ± 2.7	0.7 ± 0.4	1.6 ± 0.3	0.074 ± 0.040	0.022 ± 0.013	17.4
Clivar S4P (Located near the EF of Pennell Bank)								
27-Jan	16	0.76	15 ± 1	0.3 ± 0.1	1.8 ± 0.1	0.037 ± 0.009	0.018 ± 0.004	47.7
1-Feb	24	0.34	17 ± 2	0.5 ± 0.2	1.5 ± 0.2	0.044 ± 0.015	0.019 ± 0.007	36.3
6-Feb	41	0.78	26 ± 3	0.5 ± 0.2	1.6 ± 0.1	0.032 ± 0.008	0.009 ± 0.003	46.7
Pennell Bank								
21-Jan	02, EF	0.57	34 ± 2	0.3 ± 0.1	8.4 ± 0.6	0.068 ± 0.011	0.009 ± 0.001	127.9
23-Jan	07, CB	2.36	167 ± 16	4.0 ± 1.1	4.2 ± 0.4	0.102 ± 0.028	0.069 ± 0.019	41.9
31-Jan	21, WF	5.26	123 ± 14	4.2 ± 1.3	2.9 ± 0.8	0.116 ± 0.087	0.094 ± 0.029	29.38
8-Feb	48, CB	1.04	45 ± 3	0.9 ± 0.2	1.8 ± 0.1	0.036 ± 0.007	0.013 ± 0.003	49.74
10-Feb	64, CB	6.37	155 ± 14	5.5 ± 1.3	3.2 ± 0.3	0.113 ± 0.027	0.060 ± 0.014	28.16

Error terms are the confidence intervals of the model fit. Maximal productivity rates are shown as calculated with and without normalization to chlorophyll. The quantum yield is calculated as denoted in the text; the half saturation coefficient (Ek) is determined from Pmax and alpha. The location of each station relative to the longitudinal bank topography is noted as EF (Eastern Flank), CB (Central Bank), NB (Northern Bank) or WF (Western Flank).